TURBULENT DRAG DECOMPOSITION OVER POROUS ANISOTROPIC SUBSTRATES

Noe Faure
Department of Engineering
University of Cambridge
Trumpington Street, Cambridge CB2 1PZ
nf399@cam.ac.uk

Ricardo Garcia-Mayoral
Department of Engineering
University of Cambridge
Trumpington Street, Cambridge CB2 1PZ
r.gmayoral@eng.cam.ac.uk

ABSTRACT

We conduct Direct Numerical Simulations (DNSs) of turbulent channel flow over streamwise-aligned cylindrical fibres in the transitionally rough regime. DNS results show a modest drag reduction of a few percent followed by a drag degradation at larger sizes. This drag change is decomposed into a drag-reducing slip effect and additional Reynolds stresses, which are usually drag-increasing. For riblets, the onset of the drag-degraded regime has been attributed to a Kelvin-Helmholtz-type instability, but this has been found not to be always the case. For the present fibres, using spectral filters, we show that Kelvin-Helmholtz rollers contribute to at most 25% of the total additional drag, while dispersive stresses are negligible ($< 1\%$) for the size range under investigation, even beyond the drag-optimum location. As a consequence, we highlight the potential importance of an indirect drag contribution from non-linear interactions between Kelvin-Helmholtz rollers and the background turbulence.

Introduction

While surface roughness usually increases drag, some carefully designed textures display drag-reducing properties at small sizes. Preliminary studies by Gómez-de-Segura & García-Mayoral (2019) found that streamwise-aligned permeable substrates may yield skin-drag reduction of up to 25%, which is twice as large as the best riblets (Bechert *et al.*, 1997). The substrates of Gómez-de-Segura & García-Mayoral (2019) were characterised by a high streamwise permeability K_x with relatively low spanwise K_z and wall-normal K_y permeabilities. Gómez-de-Segura & García-Mayoral (2019) modelled the substrate as a homogeneous medium with vanishingly small pore size. The accuracy of the above model needs to be properly assessed, as there are a number of physical mechanisms it may not capture, such as the direct 'granular' effect of the texture on the flow, which may become significant at large texture size (Modesti *et al.*, 2021), the substrate's inhomogeneity at the interfacial region which may be better represented by jump boundary conditions (Zampogna & Bottaro, 2016) and other effects that we may not have anticipated.

We measure changes in drag in terms of the velocity shift ΔU^+, where the $(^+)$ superscript indicates viscous scaling. The effect of any texture far away from the wall can be reduced to a shift in the mean velocity profile $U^+(y^+)$, leaving turbulence otherwise smooth-wall-like. This 'outer-layer similarity' of wall-bounded turbulence reduces the effect of any texture on the outer flow to a change in mean streamwise velocity ΔU^+. For a given texture size L^+, this parameter ΔU^+ is Reynolds-number independent, allowing a straightforward comparison between different cases, as opposed to a friction coefficient (Gatti & Quadrio, 2016).

Provided that the texture is small enough, it is perceived as homogeneous by the overlying turbulence, and its effect on the outer flow can be entirely accounted for by an offset of the virtual origins seen by different flow components (Luchini *et al.*, 1991; Luchini, 1996; Ibrahim *et al.*, 2021). This offset of virtual origins, or slip effect, increases linearly with texture size L^+ and is related to the change in flow rate by

$$\Delta U^+ = \ell_U^+ - \ell_T^+, \tag{1}$$

where ℓ_U^+ is the slip velocity at the tip of the substrate and ℓ_T^+ is the depth of virtual origin for the overlying turbulence (Ibrahim *et al.*, 2021). For small textures ($\ell_T^+ \lesssim 5$) , this origin is identical to the spanwise protrusion height of Luchini *et al.* (1991). Drag-reducing textures ($\Delta U^+ > 0$) should therefore have a larger streamwise ℓ_U^+ than spanwise slip ℓ_T^+.

As the texture size increases, however, additional adverse physical phenomena appear which increase drag and set a drag- optimum. The precise mechanisms leading to the drag degradation are not yet fully understood (Endrikat *et al.*, 2021; Modesti *et al.*, 2021). The lack of a definitive explanation for the onset of the drag-degrading regime over permeable textures, alongside the shortcomings of theoretical approaches, motivates the present study. We therefore conduct fully-resolved, direct numerical simulations of turbulence over arrays of streamwise-homogeneous circular fibres, as illustrated in Figure 1, for different sizes L^+ near the drag-optimum.

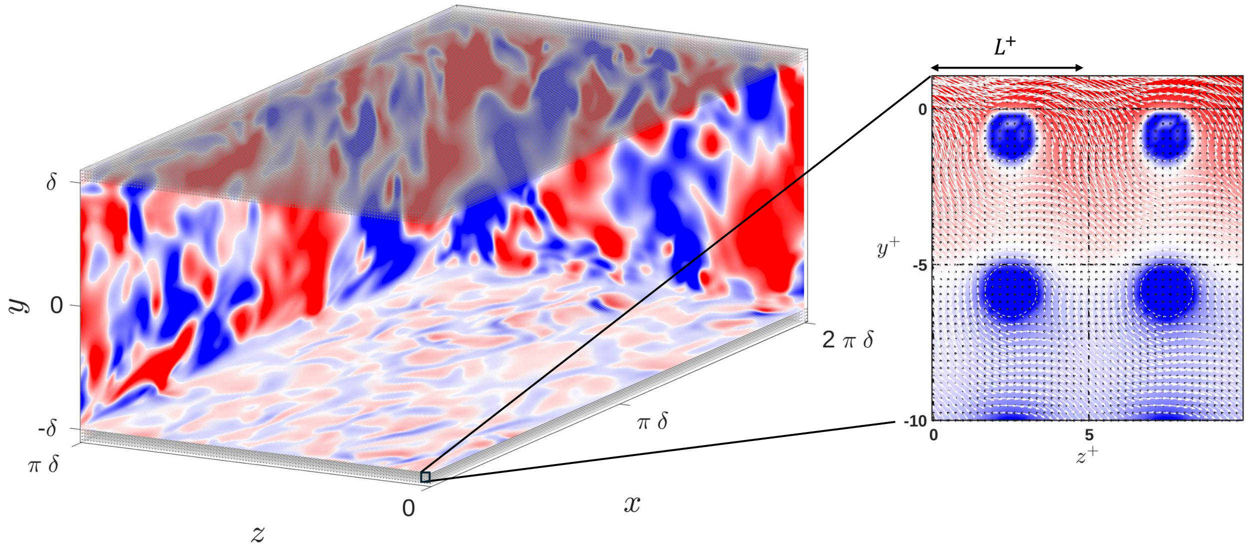

Figure 1. Computational domain with instantaneous realisations of the fluctuating wall-normal velocity from the DNS ($L^+ \approx 5$). x, z and y are the streamwise, spanwise and wall-normal directions, respectively. The zoomed-in region shows the streamwise component represented with colours ranging logarithmically from blue to red and spanwise and wall-normal components represented as a vector field. The DNS grid is shown by the solid black dots in the zoomed-in view.

Methodology

Our DNS code solves the incompressible Navier-Stokes equations in a periodic channel in the wall-parallel directions, of dimensions $2\pi\delta \times 2(\delta + k) \times \pi\delta$ in the streamwise, wall-normal and spanwise direction, where k is the substrate height and $\delta = 1$ the channel half-height from the tips of the substrate to the centre of the channel, as shown in Figure 1. The virtual origin for turbulence is obtained by linearly extrapolating the spanwise r.m.s. velocity at the substrate-channel interface, $\ell_T^+ = \frac{w'^+}{\frac{\partial w'^+}{\partial y^+}}\Big|_{y^+=\pm\delta^+}$.

A third-order Runge-Kutta scheme, combined with a fractional-step method ensuring continuity (Le & Moin, 1991), is used for time integration. The viscous terms are treated semi-implicitly, and the advective terms explicitly. The simulations are run at constant advective $CFL = 0.9$. Spatial derivatives are evaluated spectrally in the wall-parallel directions and with sixth-order compact finite differences in the wall-normal direction. The grid is staggered (Ferziger *et al.*, 2002) and stretched in the wall-normal direction, with grid spacing $\Delta y^+ \lesssim 0.3$ in the substrate region and $\Delta y^+ \lesssim 3$ in the channel core. A multi-block structure allows the use of smooth wall resolution above the roughness sublayer to alleviate the computational costs of substrate-resolved simulations with minimum impact on fidelity. The spanwise spacing in the channel core is $\Delta z^+ \approx 3$ and $\Delta z^+ \approx 0.073 - 0.22$ in the substrate region, depending on the texture size. The streamwise grid spacing is $\Delta x^+ \lesssim 8$ throughout. We use an immersed boundary method to resolve the geometry, with 7 solid points and 14 fluid points per L^+, as shown in Figure 1. The simulations are run at fixed $Re_\tau = 180$ by imposing a constant pressure gradient over the entire channel. After discarding initial transient effects, statistics are acquired for at least 40 largest eddy turnover times δ/u_τ to ensure convergence.

Results and analysis

We run DNSs over collocated arrays of cylindrical fibres for increasing texture sizes with fixed radius $r/L \approx 0.167$ and

Table 1. Simulation parameters: texture pitch L^+, wall-normal permeability $\sqrt{K_y^+}$, Δz_s^+ spanwise resolution in the substrate region, streamwise slip velocity ℓ_U^+, turbulence virtual origin ℓ_T^+, ΔU^+ change in flow rate measured from the DNSs.

Case	L^+	$\sqrt{K_x^+}$	$\sqrt{K_y^+}$	ℓ_U^+	ℓ_T^+	ΔU^+
L13	1.3	0.41	0.29	0.18	0.13	-0.18
L18	1.8	0.54	0.38	0.25	0.18	0.047
L22	2.2	0.68	0.48	0.3	0.22	0.094
L30	3.0	0.91	0.64	0.38	0.26	0.13
L34	3.4	1.0	0.73	0.43	0.30	0.31
L40	4.0	1.2	0.84	0.50	0.36	0.48
L48	4.8	1.4	1.0	0.58	0.44	0.99

anisotropy ratio $\phi_{xy} = \sqrt{K_x/K_y} = \sqrt{K_x/K_z} \approx 1.4$, which is an order of magnitude smaller than the optimal substrate of Gómez-de-Segura & García-Mayoral (2019). All substrates, listed in Table 1, are four rows deep. The resulting streamwise ℓ_x and spanwise ℓ_z slip lengths were smaller than their corresponding permeabilities $\sqrt{K_x}$ and $\sqrt{K_z}$ by roughly 50% (Table 1), which suggests that the drag estimates of Gómez-de-Segura & García-Mayoral (2019) would be overestimated by a similar factor. While the present substrate configuration therefore presents limited practical interest for drag reduction, we expect all the relevant physical mechanisms to be present. The values of ΔU^+, shown in Figure 2, present a small drag reduction at low wall-normal permeabilities, followed by a gradual drag degradation for increasing sizes. ΔU^+ follows the same trend reported for riblets (Walsh *et al.*, 1989; Bechert *et al.*, 1997) and for the modelled anisotropic permeable substrates

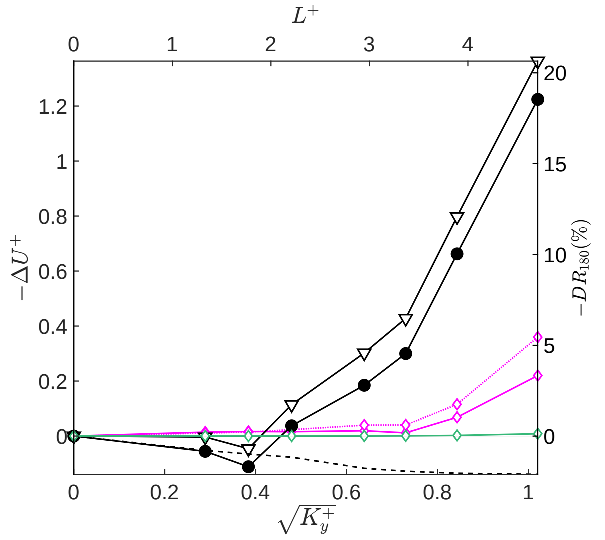

Figure 2. Drag increase $-\Delta U^+$ as a function of the wall-normal permeability $\sqrt{K_y^+}$ and the texture pitch L^+. DR_{180} stands for the skin-drag reduction at $Re_\tau = 180$. ▽, total additional Reynolds stresses ΔE_{uv}^+; - - -, contribution from the slip effect, $\ell_U^+ - \ell_T^+$; ●, ΔU^+ calculated from equation 3, as a sum of contributions from additional Reynolds stresses and slip effect; ◇, additional Reynolds stresses ΔE_{uv}^+ restricted to a fixed, Kelvin-Helmholtz spectral region; ◇ (dotted), additional Reynolds stresses ΔE_{uv}^+ restricted to a height-dependent Kelvin-Helmholtz spectral region; ◇, dispersive stresses.

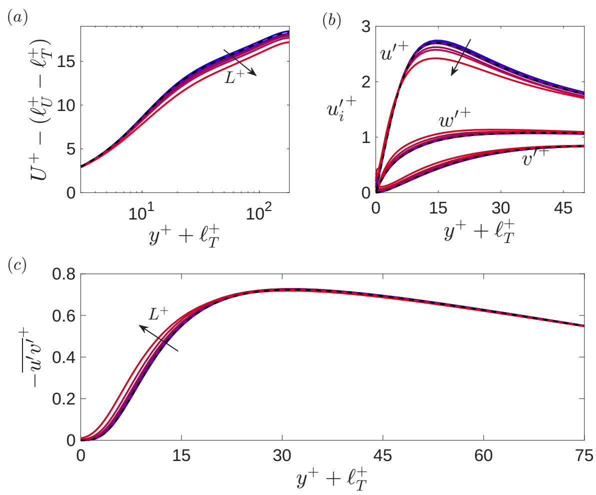

Figure 3. (*a*) Mean streamwise velocity with slip ℓ_U^+ subtracted; (*b*) r.m.s. velocity fluctuations; (*c*) Reynolds shear stresses. Texture size increases from blue to red in the direction of the arrows. The dashed black lines (- - -) are smooth-wall results for reference.

of Gómez-de-Segura & García-Mayoral (2019).

Elaborating on the idea that an optimal texture would maximise the streamwise slip while minimising the spanwise slip, as evidenced in equation 1, Abderrahaman-Elena & García-Mayoral (2017) and Gómez-de-Segura *et al.* (2018) extended previous linear stability analyses on riblets (García-Mayoral & Jiménez, 2011*b*) to anisotropic permeable substrates by modelling them as a homogeneous medium using the Darcy-Brinkman equation

$$\nabla p = -\nu \mathbf{K}^{-1}\mathbf{u} + \nu \nabla^2 \mathbf{u}, \qquad (2)$$

where $\mathbf{u} = (u, v, w)$ is the volume-averaged velocity vector, ν is the kinematic viscosity and $\mathbf{K}$ is the permeability tensor, with components K_x, K_y and K_z along its principal directions.

The linear stability analysis suggested that a single parameter K_y^+, corresponding to the substrate's wall-normal permeability, drove the amplification of the most unstable mode, a Kelvin-Helmholtz-like instability, across different substrate topologies (Gómez-de-Segura *et al.*, 2018).

Using substrate-channel interfacial conditions derived from the Darcy-Brinkman analysis, Gómez-de-Segura & García-Mayoral (2019) ran substrate-modelled DNSs for different substrate anisotropy ratios. They reported that drag degradation was caused by the onset of spanwise-coherent, Kelvin-Helmholtz rollers, as observed also over some riblets (García-Mayoral & Jiménez, 2011*a*; Endrikat *et al.*, 2021). A good collapse of their drag-reduction curves was observed when scaled with the wall-normal permeability K_y^+, at least up to the drag-optimum location $\sqrt{K_y^+}|_{opt} \approx 0.4$, suggesting further that Kelvin-Helmholtz rollers were the leading cause of drag degradation.

The present DNS data compare well with the above result, with the drag optimum occurring around $\sqrt{K_y^+}|_{opt} \approx 0.4$, even though the statistical uncertainty given the small change in drag, $\Delta U^+ \sim 0.1$, makes a precise evaluation difficult. The slip effect for $\sqrt{K_y^+} \lesssim \sqrt{K_y^+}|_{opt}$ follows approximately the expected linear trend (Luchini, 1996).

Turbulent statistics for the cases considered are compared with smooth-wall data in Figure 3, shifted by the virtual origin for turbulence ℓ_T^+. Following equation 1, this offset should collapse the turbulent statistics if turbulence remains smooth-wall-like (Ibrahim *et al.*, 2021). On the other hand, the progressive lack of collapse with increasing texture size is evidence for the departure from smooth-wall turbulence. This is chiefly noticeable on the r.m.s. velocities where a reduction in the peak value of u' alongside a mild decrease in v' and w' is observed, similarly to rough surfaces (Orlandi & Leonardi, 2006; Flores & Jimenez, 2006; Sharma & García-Mayoral, 2020). This is accompanied by a reduced mean velocity and increased Reynolds shear stresses in the near-wall region $y^+ \lesssim 30$.

Integrating twice the streamwise momentum equation and taking the difference between the permeable substrates and a smooth wall allows us to quantify the separate contributions of the slip effect and the Reynolds stresses to ΔU^+ (Gómez-de-Segura & García-Mayoral, 2019),

$$\Delta U^+ = \underbrace{U_R^+(0) - U_S^+(\ell_T^+)}_{\text{Slip effect}} + \underbrace{\int_{\ell_T^+}^{H^+} \left[\overline{u'v'}_R^+ - \overline{u'v'}_S^+\right] dy^+}_{\text{Additional Reynolds stresses}}, \qquad (3)$$

where the R and S subscripts denote the permeable substrate and smooth wall, respectively, and H^+ is a height sufficiently far above the texture for outer-layer similarity to hold. For the permeable substrate, the mean velocity at the interface is $U_R^+(0) \approx \ell_U^+$, and for the smooth wall, the mean velocity at a height ℓ_T^+ above the reference smooth wall is $U_S^+(\ell_T^+) \approx \ell_T^+$. Equation 3 highlights the leading role of additional Reynolds

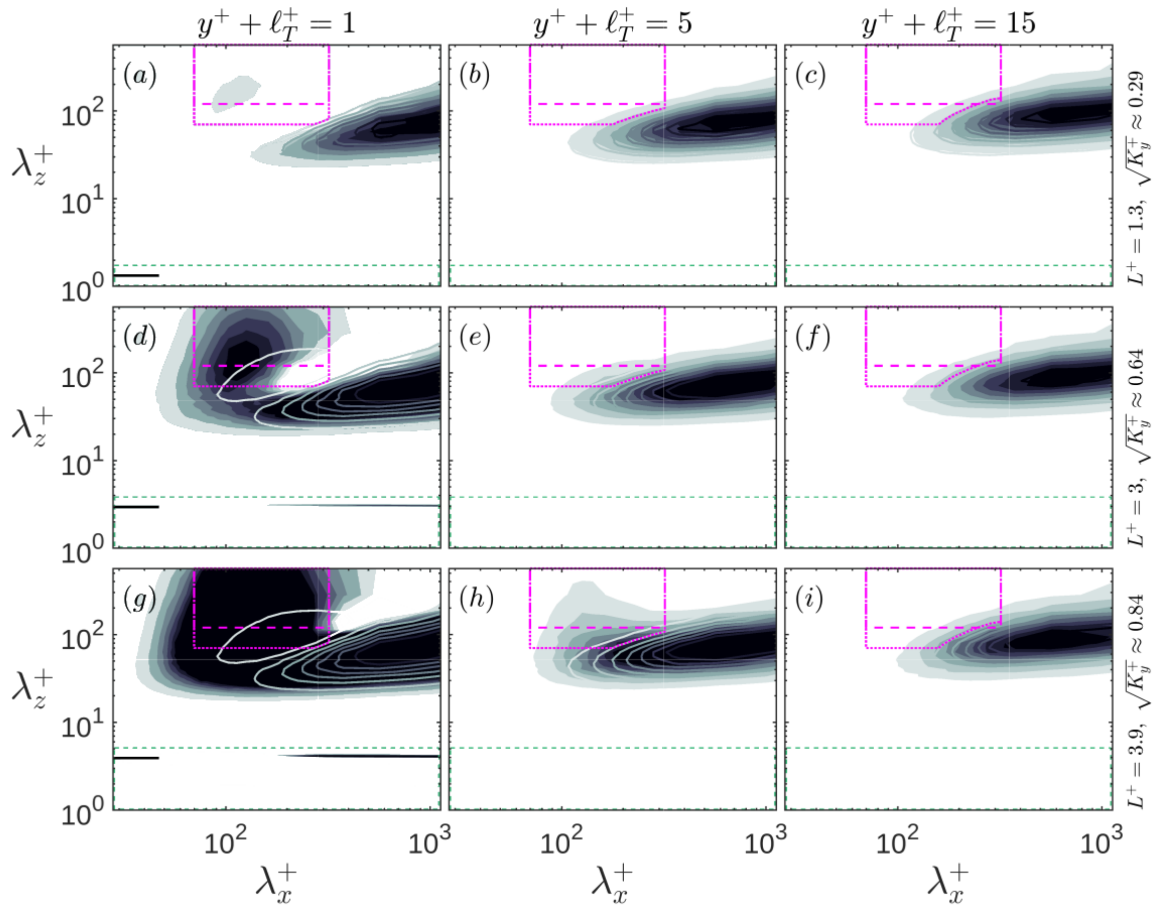

Figure 4. Pre-multiplied Reynolds stress co-spectrum $k_x k_z E_{uv}^+$ with increasing wall-normal height from left to right and increasing texture-size from top to bottom. Shaded contours; permeable substrate, line contours; smooth wall, with intensity increasing from light to dark. In each panel, contours values are the same for the smooth wall and permeable substrate. ⬚: Fixed Kelvin-Helmholtz region used in Gómez-de-Segura & García-Mayoral (2019); ⬚: height-dependent Kelvin-Helmholtz region; ⬚: dispersive stresses filter. The solid black dash marks the texture pitch L^+.

stresses, shown in Figure 3(c), in the drag degradation and reduces to equation 1 in their absence.

Further insight into the disruption of the near-wall cycle and the generation of additional Reynolds stresses is provided by the Reynolds stress co-spectra in Figure 4. We note the appearance of two new regions in the $\overline{u'v'}$ co-spectrum when compared with the smooth wall reference case. One corresponds to the Kelvin-Helmholtz rollers and has been held to be the leading cause of drag-degradation over riblets and anisotropic textures (García-Mayoral & Jiménez, 2011a,b; Gómez-de-Segura & García-Mayoral, 2019). It occupies a spectral region defined by large spanwise wavelengths, $\lambda_z^+ \gtrsim 200$ and a specific set of streamwise wavelengths, $\lambda_x^+ \approx 100-200$, and is intense only near the wall, $y^+ + \ell_T^+ < 20$. The Kelvin-Helmholtz signature appears to be present even for the smallest texture size, $L^+ = 1.3$ or $\sqrt{K_y^+} \approx 0.3$. This is consistent with the linear stability analysis of Gómez-de-Segura *et al.* (2018) and the subsequent DNSs (Gómez-de-Segura & García-Mayoral, 2019), which predict $\sqrt{K_y^+} \approx 0.4$ for the onset of the Kelvin-Helmholtz instability. For the largest texture sizes $\sqrt{K_y^+} \approx 0.8$, the Kelvin-Helmholtz signature remains visible on the co-spectra up to $y^+ + \ell_T^+ \approx 5$.

Alongside results from linear stability analyses over riblets (García-Mayoral & Jiménez, 2011b; Camobreco *et al.*, 2025), DNS for some riblet geometries have shown a prevalent effect of Kelvin-Helmholtz rollers in the drag degradation. In García-Mayoral & Jiménez (2011a), the spectral region associated with these rollers contained roughly 60% of the additional stresses, rising to $80-90$% for the substrates of Gómez-de-Segura & García-Mayoral (2019) using a smaller spectral region. More recent studies, however, have challenged the idea that Kelvin-Helmholtz rollers were the sole cause of drag degradation for anisotropic textures (Endrikat *et al.*, 2021; Modesti *et al.*, 2021; Camobreco *et al.*, 2025). For various riblet geometries, the above works showed that drag degradation occurred even with a negligible presence of spanwise rollers. Modesti *et al.* (2021) suggested that dispersive stresses, the texture-coherent secondary flow caused by the presence of individual texture elements, were then the leading drag-degrading mechanism.

The second region of additional Reynolds stresses in Figure 4 corresponds to these dispersive stresses. It lies in the vicinity of the spanwise periodicity of the texture $\lambda_z^+ \approx L^+$ and vanishes quickly away from the wall.

In agreement with the Reynolds stresses profiles in Figure 3(c), the $\overline{u'v'}$-stress distributions in Figure 4 (c,f,i) collapse above $y^+ + \ell_T^+ = 15$ for the permeable substrate and the smooth wall. Close to the wall, $y^+ + \ell_T^+ \lesssim 15$, the signature for shorter streamwise wavelengths λ_x^+ becomes more intense for the textured cases.

The contribution of the above two regions, the Kelvin-Helmholtz rollers and the dispersive stresses, to the additional Reynolds stresses in equation 3 can be quantified by partitioning the spectral domain into subregions. Starting with the dispersive stresses, the separation of scales between the texture pitch, $L^+ < 5$, and the other flow components, with $\lambda_z^+ \gtrsim 20$, makes spectral filtering suitable. We define the dispersive stresses as the region extending up to $\lambda_z^+ \lesssim 1.3L^+$, which allows us to capture the full bandwidth of interactions with the texture, as displayed in Figure 4. For the texture range considered, $L^+ < 5$, the dispersive stresses are however negligible ($< 1\%$).

Separating the Kelvin-Helmholtz rollers from the background turbulence is more challenging, as there is no clear scale separation in the co-spectrum. As a consequence, some arbitrariness is involved in the filter definition. García-Mayoral & Jiménez (2011*b*) used a spectral region defined by $70 < \lambda_x^+ < 300$ and $\lambda_z^+ > 120$, which has been used subsequently in other works (Gómez-de-Segura & García-Mayoral, 2019; Endrikat *et al.*, 2021). We propose to use a similar region except that we increase the spanwise extent of the filter down to $\lambda_z^+ > 70$ to capture a greater proportion of the Kelvin-Helmholtz signature that we may have otherwise missed, as exemplified in Figure 4(d). There is a trade-off when setting the filter dimensions between capturing more of the Kelvin-Helmholtz signature and limiting contributions from the background turbulence. As we move away from the wall, the Kelvin-Helmholtz signature weakens and the background turbulence is displaced towards larger spanwise wavelengths λ_z^+, overlapping with the Kelvin-Helmholtz region. We address this effect by employing a height-dependent filter, shown in Figure 4$(a-c)$, $(d-f)$, $(g-i)$, based on the energy contours for smooth-wall turbulence, which are here used as a surrogate for the background turbulent component in the substrate case. Results using the standard filter of García-Mayoral & Jiménez (2011*b*) and the present height-dependent one are shown in Figure 2 and can be taken as a lower and an upper bound for the direct contribution of the Kelvin-Helmholtz rollers to the additional Reynolds stresses. The results suggest that this contribution is between 10% and 25% of the total, as shown in Figure 2. Moreover, the contribution from the Kelvin-Helmholtz rollers to drag is negligible near the drag-optimum location $\sqrt{K_y^+}|_{opt} \approx 0.4$. Nevertheless, the prediction $\sqrt{K_y^+}|_{opt} \approx 0.4$, assuming the optimum is caused by the onset of Kelvin-Helmholtz rollers, appears to hold. This poses the question of whether their onset is still associated with the degradation of drag, even indirectly.

So far, we have only quantified the direct influence of the Kelvin-Helmholtz rollers on the flow, that is, with their effect circumscribed to the spectral region corresponding to the large spanwise wavelengths described earlier. One possibility is that the interscale, non-linear interaction between Kelvin-Helmholtz rollers and other flow components, as determined by the advective terms in the momentum equations (Xie *et al.*, 2024), causes the additional Reynolds stresses. To test this hypothesis, we introduce a penalty force term $\hat{\mathbf{F}} = -\Lambda(\lambda_x^+, \lambda_z^+, y^+) \cdot [\hat{u}, \hat{v}, 0]^T$ in the Navier-Stokes equations, where Λ is an inverse timescale. The forcing is restricted to the Fourier modes corresponding to the Kelvin-Helmholtz region and to the near-wall region, $y^+ + \ell_T^+ < 10$, where the rollers are most intense. The penalty force selectively suppresses the Kelvin-Helmholtz rollers, and by this, we also expect to suppress any indirect effects arising in their presence. Results for the largest texture size $\sqrt{K_y^+} \approx 1$ for different forcing strength Λ are displayed in Figure 5. In addition to suppressing the Kelvin Helmholtz region, we notice that the penalty force shifts the main region of turbulence towards increasingly larger streamwise wavelength λ_x^+ as the forcing strength Λ increases.

The penalty force should ideally have no effect on the background turbulence. To assess this, we apply the same forcing on a smooth-wall flow, which is free of Kelvin-Helmholtz rollers. The forcing has a minor effect on the E_{uu}^+ spectrum and causes a slight intensification of the other components, as shown in Figure $5(d,i,n,s)$. The spectra of the various flow components for the maximally forced cases $\Lambda T_{et} \approx 300$ over the substrate all become more smooth-wall-like and in close agreement with the forced smooth wall. Overall, the results suggests that the Kelvin-Helmholtz rollers play a key role in the generation of additional Reynolds stresses in the spectral regions not directly associated with them, and a significant contribution from indirect, non-linear interactions between the Kelvin-Helmholtz rollers and the background turbulence. Future work will be dedicated to understanding these interactions in greater detail and to quantifying them.

Conclusions

Drag-reduction by anisotropic substrates occurs in a limited range of small texture size. Larger textures trigger adverse mechanisms which contribute to the degradation of drag by increasing the Reynolds shear stresses. The exact mechanisms that increase drag are still unclear. Kelvin-Helmholtz rollers and dispersive stresses have both been proposed as the leading cause of drag degradation. To study this problem, we have run texture-resolved simulations of streamwise-aligned cylindrical fibres of texture pitch $L^+ \approx 1-5$ and permeability $\sqrt{K_y^+} \approx 0.3-1$. We have quantified the drag contribution for each component by spectrally filtering the regions of interest. The dispersive stresses were found to be negligible for the range of texture sizes considered. Kelvin-Helmholtz stresses were negligible in the drag optimum region, $\sqrt{K_y^+}|_{opt} \approx 0.4$, and contributed to roughly $15-25\%$ of the additional Reynolds stresses for the largest texture size, $\sqrt{K_y^+} \approx 1$. We have subsequently examined the contribution from non-linear interactions between the Kelvin-Helmholtz rollers and the background turbulence by selectively suppressing the spectral region corresponding to the former. The turbulent spectra of the anisotropic permeable substrates became more smooth-wall-like with increasing forcing strength, suggesting that those non-linear interactions can play a significant role in the degradation of drag. Future work will address this non-linear interaction in more depth.

REFERENCES

Abderrahaman-Elena, Nabil & García-Mayoral, Ricardo 2017 Analysis of anisotropically permeable surfaces for turbulent drag reduction. *Physical Review Fluids* **2** (11), 114609.

Bechert, Dietrich W, Bruse, Martin, Hage, W vd, Van der Hoeven, JG Th & Hoppe, G 1997 Experiments on drag-reducing surfaces and their optimization with an adjustable geometry. *Journal of fluid mechanics* **338**, 59–87.

Camobreco, Christopher J, Endrikat, Sebastian, García-Mayoral, Ricardo, Luhar, Mitul & Chung, Daniel 2025 Why do only some riblets promote spanwise rollers? *Journal of Fluid Mechanics* **1022**, A35.

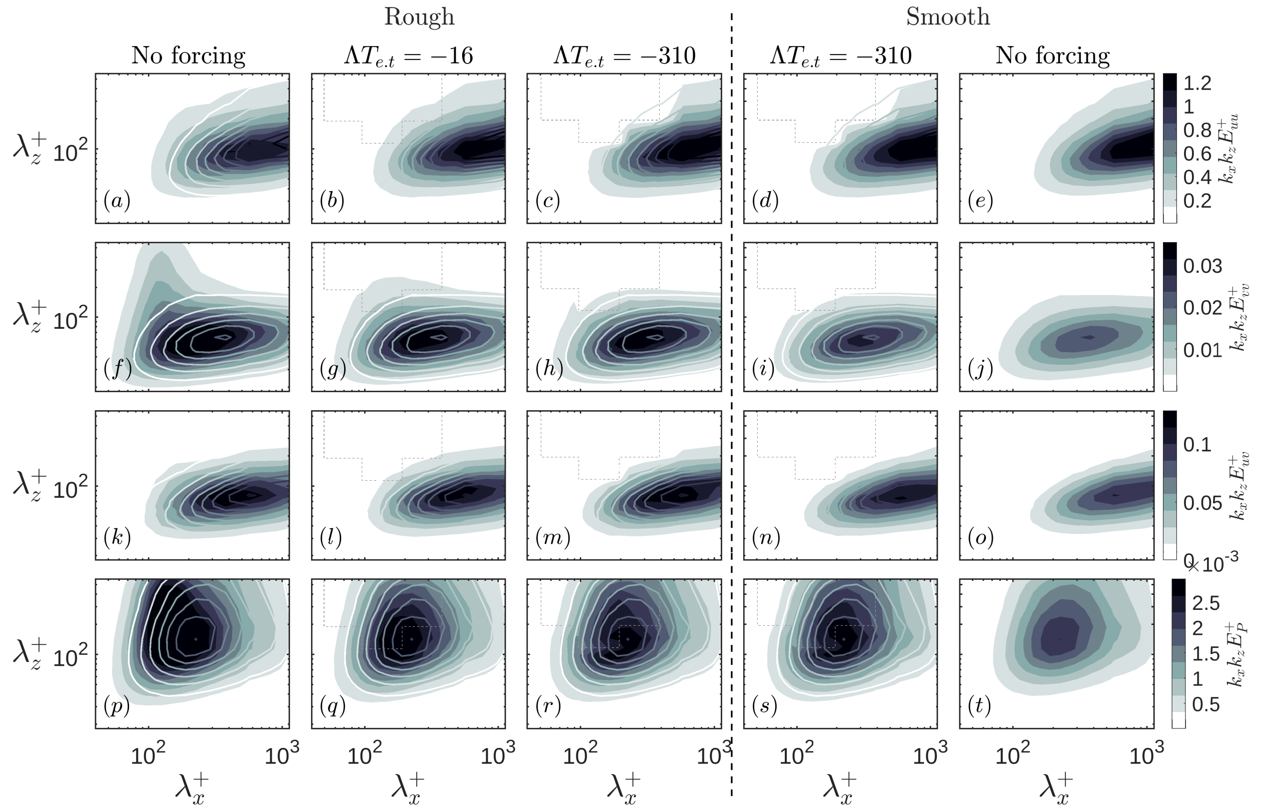

Figure 5. Pre-multiplied spectra at $y^+ + \ell_T^+ \approx 10$ for case *L*48. ⬚: Spectral region where the penalty force $\Lambda(\lambda_x, \lambda_z) \neq 0$ is applied. Shaded contours: permeable substrate, line contour: smooth wall, with increasing intensity from white to black. Contour increments are identical across a row.

Endrikat, Sebastian, Modesti, Davide, García-Mayoral, Ricardo, Hutchins, Nicolas & Chung, Daniel 2021 Influence of riblet shapes on the occurrence of kelvin–helmholtz rollers. *Journal of Fluid Mechanics* **913**, A37.

Ferziger, Joel H, Perić, Milovan & Street, Robert L 2002 *Computational methods for fluid dynamics*, , vol. 3. Springer.

Flores, Oscar & Jimenez, Javier 2006 Effect of wall-boundary disturbances on turbulent channel flows. *Journal of Fluid Mechanics* **566**, 357–376.

García-Mayoral, Ricardo & Jiménez, Javier 2011*a* Drag reduction by riblets. *Philosophical transactions of the Royal society A: Mathematical, physical and engineering Sciences* **369** (1940), 1412–1427.

García-Mayoral, Ricardo & Jiménez, Javier 2011*b* Hydrodynamic stability and breakdown of the viscous regime over riblets. *Journal of Fluid Mechanics* **678**, 317–347.

Gatti, Davide & Quadrio, Maurizio 2016 Reynolds-number dependence of turbulent skin-friction drag reduction induced by spanwise forcing. *Journal of Fluid Mechanics* **802**, 553–582.

Gómez-de-Segura, Garazi & García-Mayoral, Ricardo 2019 Turbulent drag reduction by anisotropic permeable substrates–analysis and direct numerical simulations. *Journal of Fluid Mechanics* **875**, 124–172.

Gómez-de-Segura, Garazi, Sharma, Akshath & García-Mayoral, R 2018 Turbulent drag reduction using anisotropic permeable substrates. *Flow, Turbulence and Combustion* **100** (4), 995–1014.

Ibrahim, Joseph I, Gómez-de-Segura, Garazi, Chung, Daniel & García-Mayoral, Ricardo 2021 The smooth-wall-like behaviour of turbulence over drag-altering surfaces: a unifying virtual-origin framework. *Journal of Fluid Mechanics* **915**, A56.

Le, Hung & Moin, Parviz 1991 An improvement of fractional step methods for the incompressible navier-stokes equations. *Journal of computational physics* **92** (2), 369–379.

Luchini, Paolo 1996 Reducing the turbulent skin friction. In *Computational methods in applied sciences' 96 (Paris, 9-13 September 1996)*, pp. 465–470.

Luchini, Paolo, Manzo, Fernando & Pozzi, Amilcare 1991 Resistance of a grooved surface to parallel flow and cross-flow. *Journal of fluid mechanics* **228**, 87–109.

Modesti, Davide, Endrikat, Sebastian, Hutchins, Nicholas & Chung, Daniel 2021 Dispersive stresses in turbulent flow over riblets. *Journal of Fluid Mechanics* **917**, A55.

Orlandi, Paolo & Leonardi, Stefano 2006 Dns of turbulent channel flows with two-and three-dimensional roughness. *Journal of Turbulence* (7), N73.

Sharma, Akshath & García-Mayoral, Ricardo 2020 Turbulent flows over dense filament canopies. *Journal of Fluid Mechanics* **888**, A2.

Walsh, Michael J, Sellers III, William L & Mcginley, Catherine B 1989 Riblet drag at flight conditions. *Journal of Aircraft* **26** (6), 570–575.

Xie, Wenxiong, Fairhall, Chris T & García-Mayoral, Ricardo 2024 Resolving turbulence and drag over textured surfaces using texture-less simulations: the case of slip/no-slip textures. *Journal of Fluid Mechanics* **1000**, A36.

Zampogna, Giuseppe A & Bottaro, Alessandro 2016 Fluid flow over and through a regular bundle of rigid fibres. *Journal of Fluid Mechanics* **792**, 5–35.